The Astrophysical Journal, 719:483–496, 2010 August 10 doi:10.1088/0004-637X/719/1/483

A LABOCA SURVEY OF THE EXTENDED CHANDRA DEEP FIELD SOUTH—SUBMILLIMETER PROPERTIES OF NEAR-INFRARED SELECTED GALAXIES

T. R. Greve[1], A. Weiβ[2], F. Walter[1], I. Smail[3], X. Z. Zheng[4], K. K. Knudsen[5], K. E. K. Coppin[3], A. Kovács[2], E. F. Bell[1], C. de Breuck[6], H. Dannerbauer[1], M. Dickinson[7], E. Gawiser[8], D. Lutz[9], H.-W. Rix[1], E. Schinnerer[1], D. Alexander[3], F. Bertoldi[5], N. Brandt[10], S. C. Chapman[11], R. J. Ivison[12], A. M. Koekemoer[13], E. Kreysa[2], P. Kurczynski[8], K. Menten[2], G. Siringo[2], M. Swinbank[3], and P. van der Werf[14]

[1] Max-Planck-Institut für Astronomie, 69117 Heidelberg, Germany; tgreve@mpia-hd.mpg.de
[2] Max-Planck-Institut für Radioastronomie, D-53121 Bonn, Germany
[3] Institute for Computational Cosmology, Durham University, Durham DH1 6BH, UK
[4] Purple Mountain Observatory, Chinese Academy of Sciences, Nanjing 210008, China
[5] Argelander Institute for Astronomy, University of Bonn, 53121 Bonn, Germany
[6] European Southern Observatory, Garching bei München, Germany
[7] National Optical Astronomical Observatory, Tucson, AZ 85719, USA
[8] Department of Astronomy, Yale University, New Haven, CT, USA
[9] Max-Planck-Institut für extraterrestrische Physik, 85741 Garching bei München, Germany
[10] Pennsylvania State University, Astronomy and Astrophysics 525 Davey Lab, University Park, PA 16802, USA
[11] Institute for Astronomy, Cambridge CB3 0HA, UK
[12] UK Astronomy Technology Centre, Royal Observatory, Edinburgh EH9 3HJ, UK
[13] Space Telescope Science Institute, Baltimore, MD 21218, USA
[14] Leiden Observatory, Leiden University, P.O. Box 9513, NL-2300 RA Leiden, The Netherlands
Received 2009 March 31; accepted 2010 April 20; published 2010 July 21

ABSTRACT

Using the 330 hr ESO-MPG 870 μm survey of the Extended Chandra Deep Field South (ECDF-S) obtained with the Large Apex BOlometer CAmera (LABOCA) on the Atacama Pathfinder EXperiment (APEX), we have carried out a stacking analysis at submillimeter (submm) wavelengths of a sample of 8266 near-infra-red (near-IR) selected ($K_{\rm vega} \leqslant 20$) galaxies, including 893 BzK galaxies, 1253 extremely red objects (EROs), and 737 distant red galaxies (DRGs), selected from the Multi-wavelength Survey by Yale-Chile (MUSYC). We measure average 870 μm fluxes of 0.22 ± 0.01 mJy (22.0σ), 0.48 ± 0.04 mJy (12.0σ), 0.39 ± 0.03 mJy (13.0σ), and 0.43 ± 0.04 mJy (10.8σ) for the $K_{\rm vega} \leqslant 20$, BzK, ERO, and DRG samples, respectively. For the BzK, ERO, and DRG sub-samples, which overlap to some degree and are likely to be at $z \simeq$ 1–2, this implies an average far-IR luminosity of $\sim$(1–5) $\times\ 10^{11}\ L_{\odot}$ and star formation rate (SFR) of $\sim$20–90 $M_{\odot}$. Splitting the BzK galaxies into star-forming (sBzK) and passive (pBzK) galaxies, the former is significantly detected (0.50 ± 0.04 mJy, 12.5σ) while the latter is only marginally detected (0.34 ± 0.10 mJy, 3.4σ), thus confirming that the sBzK and pBzK criteria to some extent select obscured, star-forming, and truly passive galaxies, respectively. The $K_{\rm vega} \leqslant 20$ galaxies are found to contribute 7.27 ± 0.34 Jy deg^{-2} ($16.5\% \pm 5.7\%$) to the 870 μm extragalactic background light (EBL). sBzK and pBzK galaxies contribute 1.49 ± 0.22 Jy deg^{-2} ($3.4\% \pm 1.3\%$) and 0.20 ± 0.14 Jy deg^{-2} ($0.5\% \pm 0.3\%$) to the EBL. We present the first delineation of the average submm signal from the $K_{\rm vega} \leqslant 20$ selected galaxies and their contribution to the submm EBL as a function of (photometric) redshift, and find a decline in the average submm signal (and therefore IR luminosity and SFR) by a factor $\sim$2–3 from $z \sim 2$ to $z \sim 0$. This is in line with a cosmic star formation history in which the star formation activity in galaxies increases significantly at $z \gtrsim 1$. A linear correlation between the average 24 μm and 870 μm flux densities is found for the $K_{\rm vega} \leqslant 20$ galaxies with 24 μm fluxes $\lesssim$350 μJy (corresponding to $L_{\rm IR} \simeq 1.5 \times 10^{12}\ L_{\odot}$ at $z \simeq 2$), while at higher 24 μm fluxes there is no correlation. This behavior suggests that star formation, and not active galactic nuclei (AGNs), is in general responsible for the bulk of the mid-IR emission of $L_{\rm IR} \lesssim 1.5 \times 10^{12}\ L_{\odot}$ systems, while in more luminous systems the AGN makes a significant contribution to the 24 μm emission. By mapping the stacked 870 μm signal across the $B - z$ versus $z - K$ diagram we have confirmed the ability of the sBzK selection criterion to select star-forming galaxies at $z > 1$, although our analysis suggests that the subset of sBzK galaxies which are also EROs are responsible for >80% of the submm emission from the entire sBzK population.

Key words: cosmology: observations – galaxies: evolution – galaxies: formation – galaxies: high-redshift

1. INTRODUCTION

Extragalactic blank-field submillimeter (submm) surveys have been carried out since the advent of SCUBA (Holland et al. 1999) more than a decade ago, and have provided us with a unique view of intense, dust-cloaked star formation events at high redshifts (e.g., Blain et al. 2002). Yet such observations have so far only pinpointed the most luminous high-z galaxies, due to the limitations in sensitivity and resolution imposed by present-day (sub)mm facilities. It is now well established that the bright ($\gtrsim$5 mJy at 850 μm) submm sources uncovered by these surveys primarily reside in the redshift range $z \simeq$ 1.5–3.5 (Chapman et al. 2003, 2005) and account for $\sim$20%–30% of the extragalactic background light (EBL) at 850 μm (Barger et al. 1998, 1999; Hughes et al. 1998; Coppin et al. 2006). Surveys that make use of galaxy clusters' gravitational amplification of the background source plane have uncovered a number of faint ($S_{850\,\mu{\rm m}} \gtrsim 2$ mJy) sources and resolved up to 80% of the background (Smail et al. 1997, 2002a; Blain et al. 1999; Cowie et al. 2002; Chapman et al. 2002; Knudsen et al. 2008).

However, we know little about the nature and redshift distribution (Smail et al. 1997, 2002a) of the population below ∼5 mJy due in part to the difficulty of identifying counterparts in the radio.

The recent advent of large format near-IR cameras has revealed populations of moderately star-forming galaxies at $z \simeq 1$–3 that are more numerous than the (sub)mm selected systems, and more representative of the bulk population at these epochs (e.g., Cimatti et al. 2002; Lawrence et al. 2007). The rest frame near-IR is arguably the best wavelength range to undertake such surveys at—as, in comparison with UV and optical surveys, it is less sensitive to the effects of age and dust on the stellar population, and thus more closely provides a selection based on stellar mass.

Well-known examples of near-IR color-selected galaxies are the populations of extremely red objects (EROs; Elston et al. 1988; McCarthy et al. 1992; Hu & Ridgway 1994), distant red galaxies (DRGs; Franx et al. 2003; van Dokkum et al. 2003), and the so-called BzK galaxies (Daddi et al. 2004). These populations are selected according to different optical/near-IR color criteria, which pick out systems at different, but overlapping, redshift ranges. The color criteria are often designed to straddle the 4000 Å break (including the Balmer break at 3646 Å), characteristic of evolved, metal-enriched galaxies that are old enough that OB-stars do not dominate the light. The same color criteria, however, will also select dusty, star-forming galaxies at virtually any redshift. Thus, near-IR color-selected galaxy populations are typically a mix of actively star-forming galaxies and old, evolved systems, which means additional color criteria and/or spectral analysis has to be applied in order to separate the two. Clearly, submm observations offer a unique way of distinguishing between star-forming and passive near-IR galaxies.

At present, however, the bulk of near-IR color-selected galaxies are too faint for individual detection by large format (sub)mm surveys, and for the moment, therefore, the only way forward is to study their average (sub)mm/far-IR properties by means of stacking techniques. A handful of such studies have been carried out to date, characterizing the average submm signal of near-IR selected galaxies and their contribution to the EBL at submm wavelengths (Webb et al. 2004; Daddi et al. 2005; Knudsen et al. 2005; Wang et al. 2006; Takagi et al. 2007). Yet most of these stacking analyses have been of relatively small samples of galaxies, and as a consequence have had to average their submm properties over the entire redshift range from which they are selected (which is often substantial; $z \sim 1$–3). A robust delineation of the submm signal of near-IR selected galaxies as a function of redshifts has therefore been lacking, and as a consequence we do not know how the dust-enshrouded star formation in these galaxies evolve with cosmic epoch.

The Extended Chandra Deep Field South (ECDF-S), a $30' \times 30'$ region centered on the smaller GOODS-S/CDF-S field (Giavalisco et al. 2004), is one of the most intensively studied extragalactic fields in the southern sky. In addition to X-ray observations with *Chandra* (Alexander et al. 2003; Lehmer et al. 2005; Luo et al. 2008), the EDCF-S has been targeted in a large number of optical and near-IR filter passbands from the ground as part of COMBO-17 (Wolf et al. 2001) and MUSYC (Gawiser et al. 2003), and with *HST*/ACS as part of GEMS (Rix et al. 2004). Furthermore, deep mid-IR imaging has been provided by the *Spitzer* IRAC/MUSYC Public Legacy in ECDF-S (SIMPLE; Damen et al. 2009), and the *Spitzer*/MIPS Far-Infrared Deep Extragalactic Legacy Survey (FIDEL; Dickinson et al. 2007; see also http://irsa.ipac.caltech.edu/data/SPITZER/FIDEL). To study the submm properties of the sources in the ECDF-S, we have undertaken a large ESO-MPG survey (Coppin et al. 2009; Weiß et al. 2009) using the LABOCA 870 μm camera (Siringo et al. 2009) mounted on the Atacama Pathfinder Experiment (APEX) and combined the data with the already existing multi-wavelength data available for this field.

Throughout this paper, we adopt a flat cosmology with $\Omega_M = 0.27$, $\Omega_\Lambda = 0.73$, and $h = 0.71$ (Spergel et al. 2003).

2. THE SUBMM DATA

Observations were carried out using the 295 horn-bolometer array LABOCA on APEX (Siringo et al. 2009, and are discussed in detail in Weiß et al. 2009). The bolometers are AC-biased, operated in total power mode, and distributed in an hexagonal configuration over the 11.′4 field of view. The center frequency of LABOCA is 345 GHz and its passband has an FWHM of ∼60 GHz. The measured angular resolution is 19.″2 (FWHM). The observations were carried out between 2007 May and 2008 November in mostly excellent weather conditions (PWV typically 0.5 mm corresponding to a zenith opacity of 0.2 at the observing wavelength). The mapping pattern was chosen to give a uniform coverage across a $30' \times 30'$ area centered at RA: $03^h32^m29^s$, decl.: $-27°48'47''$ (J2000).

Mapping was performed by alternating rectangular on-the-fly scans with a raster of spiral patterns. For the latter mode the telescope traces out spiral pattern scans with radii between $2'$ and $4'$ at 16 and 9 positions (the raster) spaced by $600''$ in azimuth and elevation. The scanning speed was typically between 2 and 3 arcmin per second.

Calibration was achieved through observations of Mars, Uranus, and Neptune as well as secondary calibrators and was found to be accurate to within 8.5%. The atmospheric attenuation was determined via skydips every ∼2 hr as well as from independent data from the APEX radiometer which measures the line-of-sight water vapor column every minute. Focus settings were typically determined once per night and checked during sunrise. Pointing was checked on nearby quasars PMNJ0457−2324, PMNJ0106−4034, and PMNJ0403−3605 and found to be stable within $3''$.

The data was reduced using the BoA reduction package (F. Schuller et al. 2010, in preparation; full details about the data reduction and map making procedure are given in Weiß et al. 2009). Briefly speaking, individual maps were co-added (noise weighted) and the final map was beam smoothed, resulting in a spatial resolution of $27''$ (FWHM). In order to remove any remaining large-scale structure in the map, a smoothed version of the map (in which significant detections had been blanked out beforehand) was subtracted (see also discussion in Section 4.3). The total on-source observing time in the data used for this analysis is 200 hr (330 hr including overheads) and the average rms across the entire $30' \times 30'$ field is 1.2 mJy beam^{-1}, making it the largest contiguous (sub)mm survey ever undertaken at this depth (cf. Coppin et al. 2006; Bertoldi et al. 2007).

3. NEAR-IR SELECTED GALAXIES

We use the Wide MUSYC public data release of *UBVRIzJHK* catalogs in the ECDF-S to construct samples of near-IR selected galaxies (Taylor et al. 2009).[15] The MUSYC survey covers the

[15] The catalog is available at http://www.astro.yale.edu/MUSYC/.

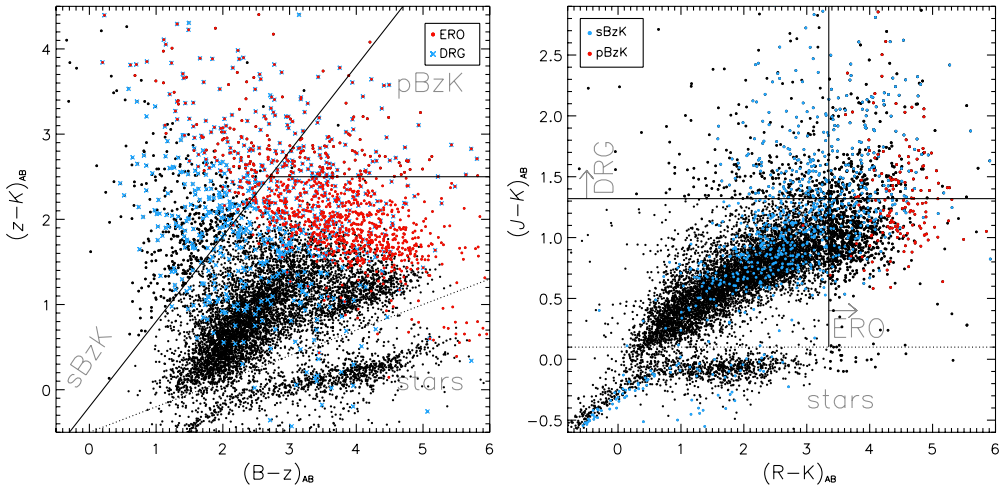

Figure 1. Color–magnitude diagrams illustrating the selection criteria for the BzK, ERO, and DRG samples. Left: the BzK diagram (Daddi et al. 2004) showing the sBzK and pBzK regions and the location of sources selected according to the ERO and DRG criteria. Right: RJK diagram showing the ERO and DRG regions and the location of the sources fulfilling the sBzK and pBzK color criteria. Sources below the dotted lines in either diagram were deemed to be stars and therefore discarded from the analysis. Note this includes a number of sources formally selected as either BzK, ERO, or DRG galaxies (see Section 3). The diagrams show the significant overlap between the different near-IR selected populations.

central $30' \times 30'$ of the ECDF-S and reaches 5σ point source sensitivities in the near-IR of $J_{AB} = 22.7$ and $K_{AB} = 22.0$, respectively (see Gawiser et al. 2006 for a detailed description of the MUSYC survey).

We defined our sample as sources with $K_{vega} \leqslant 20$ (corresponding to $K_{AB} \leqslant 21.9$, i.e., we have assumed a VEGA-AB offset of 1.9 in the K band). This magnitude cutofff was chosen since the MUSYC survey is close to 100% complete at this depth, and since other studies have adopted the same magnitude limit, thus facilitating a direct comparison. Contamination by stars was accounted for by removing objects lying on the stellar loci in the $(z - K)_{AB}$ versus $(B - z)_{AB}$ or $(J - K)_{AB}$ versus $(R - K)_{AB}$ diagrams (hereafter referred to as BzK and RJK diagrams—Figure 1). As shown in Figures 1(a) and (b), a non-negligible fraction of sources that appear as normal galaxies in the BzK diagram end up in the stellar region in the RJK diagram and vice versa. These sources were all poorly fit ($\chi^2/\nu_{dof} > 100$) by galaxy spectral energy distribution (SED) templates, thus strongly suggesting that they are in fact stars and illustrating the need to remove both stellar loci from the sample. This left us with a total sample of 8266 $K_{vega} \leqslant 20$ selected galaxies. From this sample, subsets of BzK galaxies, extremely red objects (EROs), and distant red galaxies (DRGs) were extracted as described below.

Applying the star-forming and passive BzK criteria, namely BzK $= (z - K)_{AB} - (B - z)_{AB} \geqslant -0.2$ for sBzK galaxies, and BzK < -0.2 and $(z - K)_{AB} > 2.5$ for pBzK galaxies (Daddi et al. 2004), to our $K_{vega} \leqslant 20$ catalog defined above, we obtained samples of 744 sBzK and 149 pBzK galaxies.[16] Sources that were undetected at the 1σ level in both B and z were not included. Furthermore, sources formally belonging to the sBzK region but that were undetected in B, thus having $B - z$ lower limits only, were discarded, as were sources in the pBzK region with lower limits in $z - K$. A total of 1253 EROs were selected from our $K_{vega} \leqslant 20$ sample using the standard criterion, i.e., $(R-K)_{AB} \geqslant 3.35$ (equivalent to $(R-K)_{vega} \gtrsim 5$; Elston et al. 1988; McCarthy et al. 1992; Hu & Ridgway 1994). Finally, the selection of DRGs was done by applying the color cut $(J - K)_{AB} > 1.32$ (Franx et al. 2003). In total, 737 DRGs with $K_{vega} \leqslant 20$ were selected in this way.

3.1. Overlap Between BzK, ERO, and DRG Samples

In this paper, we aim to determine the contribution to the submm background from $K_{vega} \leqslant 20$ galaxies, as well as the sub-samples of BzKs, EROs, and DRGs and their joint contributions, and it is therefore important to determine the degree of overlap between these populations. The overlaps in terms of percentages are given in Table 1.

From Figure 2 it is seen that BzK, ERO, and DRG galaxies only start to contribute significantly (>1%) to the full sample for $K_{AB} \gtrsim 20$. Even so, more than half of the full sample does not fall within the BzK/ERO/DRG classifications at these faint flux levels. Of the full $K_{vega} \leqslant 20$ sample, 6269 sources (corresponding to ∼76%) do not classify as BzKs, EROs, or DRGs.

The locations of the various samples in the BzK and RJK diagrams are shown in Figure 1. The DRGs are seen to be spread out across the BzK diagram, while the EROs lie in a much more well-defined region of the BzK diagram. EROs and DRGs make up about 30% and 36% of the sBzKs, respectively. Similarly, we find that EROs and DRGs constitute 98% and 44% of the pBzK sample, respectively. Clearly, pBzK galaxies are much more often selected as EROs than is the case for sBzKs, while the occurrence of a pBzK or sBzK galaxy being classified as a DRG is about the same. Turning to the RJK diagram we see that the sBzK galaxies are much more spread out than the pBzKs. About 18% and 37% of EROs and DRGs, respectively, are made up of sBzK, while pBzKs make up about 12% and 9% of the two populations.

The overlaps between BzK, ERO, and DRG galaxies have been discussed in detail in other studies (e.g., Reddy et al. 2005; Grazian et al. 2007; Takagi et al. 2007; Lane et al. 2007). The most statistically significant study was carried out by Lane et al. (2007) who used the UKIRT Infrared Deep Sky Survey (UKIDSS) Ultra Deep Survey Early Data Release (UDS EDR) to study large samples of BzK, ERO, and DRG galaxies. For samples selected down to $K_{AB} = 21.2$, which is close to our magnitude cutoff, they found sBzK:ERO and pBzK:ERO ratios

[16] We matched the stellar sequence in the BzK diagram with that of Daddi et al. (2004) using $(z - K)_{D04} = (z' - K) - 0.2$.

Table 1
The Total Number of Sources in Each Sample (Given in Parentheses in the First Column of Each Line), Followed by the Percentages Contributed by the Other Samples

Galaxy Type	sBzK	pBzK	ERO	DRG	sBzK+pBzK	ERO+DRG
$K_{\rm vega} \leqslant 20$ (8266)	9%(744)	1.8%(149)	15.2%(1253)	8.9%(737)	10.8%(893)	19.6%(1620)
sBzK (744)	100%(744)	0%(0)	30.4%(226)	36.2%(269)	83.3%(744)	49.7%(370)
pBzK (149)	0%(0)	100%(149)	98.0%(146)	43.6%(65)	16.7%(149)	98%(146)
ERO (1253)	18.0%(226)	11.7%(146)	100%(1253)	29.5%(370)	29.7%(372)	100%(1253)
DRG (737)	36.5%(269)	8.8%(65)	50.2%(370)	100%(737)	45.3%(334)	100%(737)
sBzK+pBzK (893)	83.3%(744)	16.7%(149)	41.7%(372)	37.4%(334)	100%(893)	57.8%(516)
ERO+DRG (1620)	22.8%(370)	9.0%(146)	63.0%(1253)	37.0%(737)	31.9%(516)	100%(1620)

Note. The latter are also given as absolute numbers in parentheses.

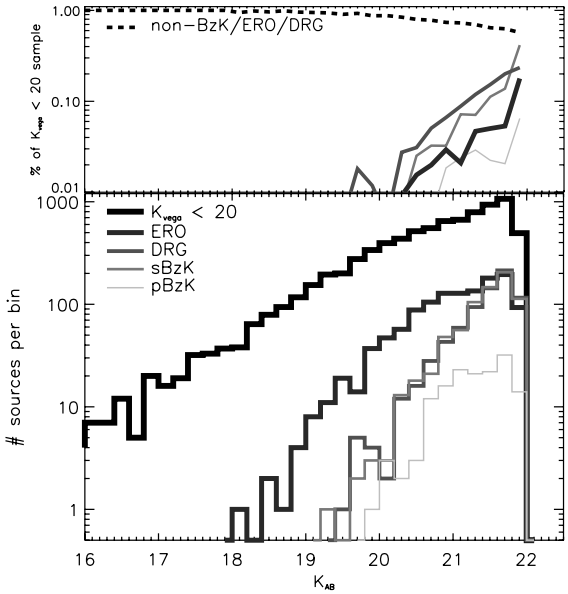

Figure 2. Top: percentages, i.e., fraction of the full $K_{\rm vega} \leqslant 20$ sample, of the BzK, ERO, and DRG samples, as well as the non-BzK/ERO/DRG sample (dashed line) as a function of their $K_{\rm AB}$ magnitude. Bottom: the number distribution of sources as a function of their $K_{\rm AB}$ magnitude. The distributions for the full sample as well as the BzK, ERO, and DRG samples are shown in order to illustrate the overlap between the different populations. While the BzK, ERO, and DRG samples start making up a non-negligible fraction of the parent sample for $K_{\rm AB} \gtrsim 20$, even at the faintest magnitudes more than half of the sources from the parent sample do not fall within any of these three classifications.

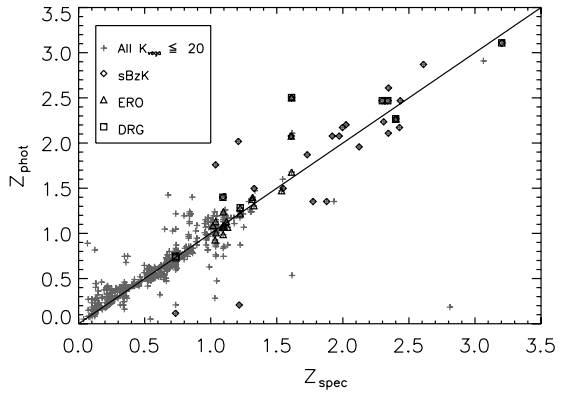

Figure 3. Photometric vs. spectroscopic redshifts for the sources in the full $K_{\rm vega} \leqslant 20$ sample, and the sBzK/pBzK, ERO, and DRG sub-samples which have spectroscopic redshifts (see Section 3.2). The normalized median absolute deviation of $\Delta z = z_{\rm phot} - z_{\rm spec}$ (see Brammer et al. 2008) is $\simeq$0.037 for $z \leqslant 1.5$ and $\simeq 0.079$ for $z > 1.5$.

of 32% and 95%, respectively, i.e., in excellent agreement with our values. They also find that about 30% of DRGs are sBzK, again in good agreement with our findings (see also Reddy et al. 2005).

3.2. Redshift Distributions

The sample was correlated against publicly available spectroscopic redshift surveys (Szokoly et al. 2004; Vanzella et al. 2005, 2006, 2008; Popesso et al. 2009; Kriek et al. 2008). Using only the most reliable spectroscopic redshifts from these surveys, we extracted 2341 redshifts, the majority of which lie within the CDF-S region. A total of 546 galaxies from our sample were matched to a spectroscopic redshift. Of these, 28 were sBzK, 21 were ERO, and 10 were DRG galaxies. The fact that no pBzK galaxies were identified with a spectroscopic redshift is not too surprising since these are in all likelihood old, evolved galaxies with optical spectra devoid of emission features, thus making it difficult to obtain robust spectroscopic redshifts (cf. Kriek et al. 2006; Cimatti et al. 2008). Sources with spectroscopic redshifts were used as a test sample to optimize input parameters for the photometric redshift code EAZY (Brammer et al. 2008). The code works by fitting non-negative linear combinations of galaxy spectra to the observed SEDs, which in our case consisted of nine MUSYC filter bands.

The resulting photometric redshifts are compared against their spectroscopic counterparts in Figure 3. The normalized median absolute deviation of $\Delta z = z_{\rm phot} - z_{\rm spec}$ (see Brammer et al. 2008) is $\simeq$0.037 for $z \leqslant 1.5$ and $\simeq 0.079$ for $z > 1.5$. Significant outliers, which we define to be sources with $|\Delta z|/(1 + z_{\rm spec})$ five times greater than the median, make up $\sim$9% of the total sample. These numbers are consistent with the typical performances of photometric redshift codes (e.g., Bolzonella et al. 2000; Quadri et al. 2007; Brammer et al. 2008).

Adopting the parameters for the test sample, photometric redshifts were derived for the remainder of the sample without spectroscopic redshifts. The redshift distributions of the full $K_{\rm vega} \leqslant 20$ sample as well as the BzK, ERO, and DRG samples are shown in Figure 4, where we also compare with two other photometric redshift distributions obtained from: (1) the MUSYC *UBVRI* and deep *JHK* imaging of the three $10' \times 10'$ fields HDFS1/S2, MUSYC 1030 and 1255 (Quadri et al. 2007, hereafter Q07), and (2) deep $BVRi'z'JK$ imaging of 1113 arcmin^2 in the Ultra-Deep Survey (UDS) portion of the United Kingdom Infrared Telescope Deep Sky Survey (UKIDSS; Dunne et al. 2009, hereafter D09).

The BzK selection criteria are defined to select galaxies in the redshifts range $1.4 < z < 2.5$ (Daddi et al. 2004), yet both

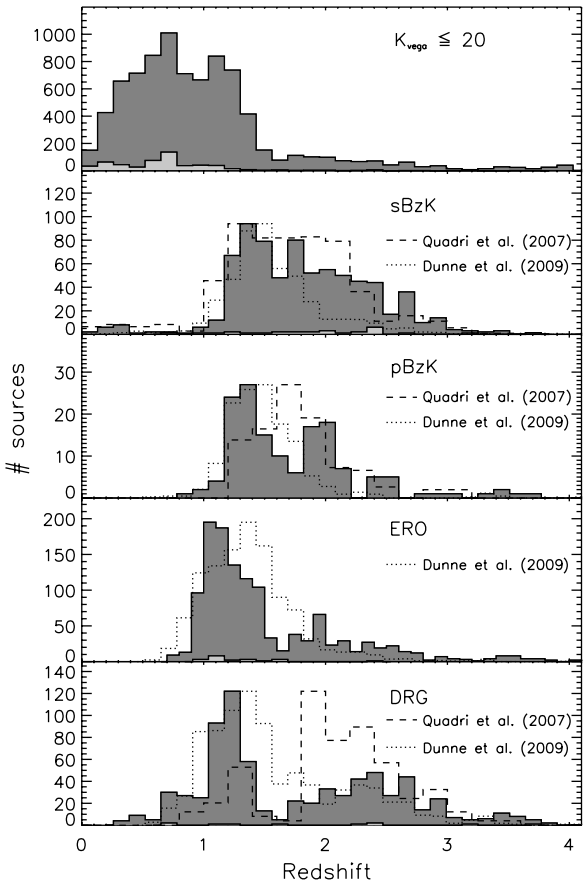

Figure 4. Top to bottom: redshift distributions of the $K_{\rm vega} \leqslant 20$, sBzK, pBzK, ERO, and DRG samples, respectively (dark gray histograms). Spectroscopic redshifts are shown as light gray histograms. Also shown are the photometric redshift distributions of the $K_{\rm vega} \leqslant 20$ sBzK, pBzK, and DRG samples by Q07, as well as of the $K_{\rm vega} \leqslant 20$ selected samples by D09. The Q07 and D09 distributions have been scaled to match the peaks of our distributions. Given the uncertainties, our $K_{\rm vega} \leqslant 20$ BzK, ERO, and DRG redshift distributions are in good agreement with those of Q07 and D09.

the sBzK and pBzK redshift distributions extend below and above this range. Of the sBzK galaxies, 66% lie in the range $1.4 < z < 2.5$, while 22% are at $z < 1.4$ and 12% at $z > 2.5$. For the pBzK galaxies, the corresponding percentages are 60%, 31%, and 9%, respectively. Both Q07 and D09 find similar fractions for their samples of $K_{\rm vega} \leqslant 20$ galaxies, suggesting that the BzK criteria select galaxies across a somewhat broader redshift range ($1 \lesssim z \lesssim 3.5$). The redshift distribution of EROs is seen to peak strongly at $z \simeq 1.1$ with a tail extending to $z \sim 3.5$. This is in line with photometric and spectroscopic surveys which have shown that the redshift distribution of EROs peaks around $z \simeq 1.2$ (Cimatti et al. 2003; Yan et al. 2004). The redshift distribution of $K_{\rm vega} \leqslant 20$ EROs derived by D09 peaks at slightly higher redshifts ($z \sim 1.4$), but overall appears similar to ours. The DRG distribution shows prominent peaks at $z \simeq 1.2$ and $z \simeq 2$, with the former being the most dominant. A similar bimodality is also apparent in the $K_{\rm vega} \leqslant 20$ DRG sample by Q07, although the dominant peak in their distribution lies at $z \simeq 2$. The distribution by D09 broadly resembles ours, with a prominent peak at $z \simeq 1.2$ followed by a significant high-z tail. Overall, therefore, our redshift distributions are consistent with those of Q07 and D09, given the uncertainties associated with photometric redshift derivation, and the effects of field-to-field variations.

4. 870 μm STACKING

In order to estimate the average 870 μm fluxes for the above excised catalogs of near-IR galaxies, we stack the 870 μm flux values at their near-IR positions in the LABOCA map.

4.1. Submm-bright Near-IR Selected Galaxies

First, however, we need to identify any galaxies that are associated with robust LABOCA sources, which we take to be mean sources detected at $\geqslant 3.7\sigma$ significance (126 in total; see Weiß et al. 2009 for details). To this end, we adopt a search radius of 12.″8 around each LABOCA source, which corresponds to the 95% confidence search radius given the FWHM = 19″ beam. For a galaxy to qualify as a near-IR counterpart to a LABOCA source we furthermore require that $z > 0.8$. This cut is motivated by the observed redshift distribution of submm galaxies which shows that $\lesssim$3% are at $z < 0.8$ (Chapman et al. 2005). If more than one galaxy meets these criteria for a given LABOCA source, we adopt the one closest to the submm source. In this manner, we find 57 submm-near-IR associations from the $K_{\rm vega} \leqslant 20$ sample. Of these, 19/2 sources are classified as sBzK/pBzK galaxies and 25 as EROs (of which 13 are also DRGs). Ten of the nineteen sBzK galaxies are also EROs and of those, nine are DRGs. Both pBzK galaxies are EROs and also DRGs. As a safeguard against contamination, these submm-bright near-IR sources were removed from the stacking analysis, although their contribution was included (in a variance-weighted fashion) in the final tally of average submm flux.

4.2. Stacking and Deblending Technique

Next, we proceeded to perform a stacking analysis of the remaining submm-undetected near-IR selected galaxies. Due to the slightly varying noise across the map, the average 870 μm flux ($\langle S_{870\,\mu{\rm m}}\rangle$) and noise ($\langle \sigma_{870\,\mu{\rm m}}\rangle$) values were calculated as the variance-weighted mean, i.e.,

$$\langle S_{870\,\mu{\rm m}}\rangle = \frac{\sum_i S_i/\sigma_i^2}{\sum_i 1/\sigma_i^2} \quad (1)$$

and

$$\langle \sigma_{870\,\mu{\rm m}}\rangle = \frac{1}{\sqrt{\sum_i 1/\sigma_i^2}}, \quad (2)$$

where S_i and σ_i are the 870 μm flux and rms noise pixel values at the near-IR position of the ith source in the stack, respectively. To avoid the stack being contaminated by robust 870 μm sources, the stacking was performed on a "residual" version of the LABOCA map in which all of the 126 870-μm sources uncovered at $\geqslant 3.7\sigma$ (Weiß et al. 2009) had been subtracted using a scaled beam profile.

An important aspect of any stacking analysis performed on maps with coarse angular resolution is the issue deblending sources that lie within a single resolution element. For example, if a BzK galaxy has a neighbor, A, within a LABOCA beam, we have to calculate the 870 μm flux contribution from A to the position of the BzK galaxy. Now, if A also has a neighbor, B, within a LABOCA beam (which is not necessarily a neighbor to the BzK galaxy), then the contribution from B to A will affect A's contribution to the BzK galaxy and will have to be included in the deblending. If B has no other neighbors other than A, then the process stops there, but if B has another neighbor, C, its contribution will also have to be factored into the deblending, and so on. In this way, "chains" of neighboring sources are

constructed for every source, and the entire "chain" of neighbors must be included in the deblending procedure.

Of the full $K_{\rm vega} \leqslant 20$ sample, 5985 sources (i.e., 72% of the sample) are involved in such a "chain" of two or more galaxies, and thus must be deblended. We correct for the blending of sources by assuming Gaussian sources with FWHMs equal to the LABOCA beam. This method is similar to the one adopted by Webb et al. (2004), although they (and subsequent submm stacking studies) did not take into account the effects from neighbors' neighbors (and so on) as discussed above. Our study is the first stacking analysis that has adopted this "global" deblending scheme. A simple illustrative example of the latter where only four sources are involved is given Figure 5, where A itself has a neighbor, B, within a LABOCA beam, which in turn has a neighbor C. Neither B nor C is within the LABOCA beam as measured from the BzK galaxy's position. In this case, we have to calculate C's contribution to B, and B's contribution to A, in order to correctly calculate A's contribution to the BzK galaxy, and the system of equations to be solved is therefore

$$f_{\rm BzK} = I_{\rm BzK} + I_{\rm A} e^{-r^2_{\rm BzK,A}/(2\sigma^2)}, \quad (3)$$

$$f_{\rm A} = I_{\rm A} + I_{\rm BzK} e^{-r^2_{\rm BzK,A}/(2\sigma^2)} + I_{\rm B} e^{-r^2_{\rm B,A}/(2\sigma^2)}, \quad (4)$$

$$f_{\rm B} = I_{\rm B} + I_{\rm A} e^{-r^2_{\rm B,A}/(2\sigma^2)} + I_{\rm C} e^{-r^2_{\rm C,A}/(2\sigma^2)}, \quad (5)$$

$$f_{\rm C} = I_{\rm C} + I_{\rm B} e^{-r^2_{\rm B,C}/(2\sigma^2)}, \quad (6)$$

where I and f are the measured and deblended fluxes at the relevant positions, respectively, and r are the distances between the sources. In order to estimate the error one makes by only deblending the fluxes from neighbors within a beam and not taking into account neighbors' neighbors etc., we ran the stacking analysis under both scenarios. We find that the deblending scheme by Webb et al. (2004) can overestimate the fluxes by $\sim$10% compared to the scheme described in this paper, but more typically the error is at the $\sim$5% level. We emphasize that one has to not only deblend neighbors within a certain galaxy population, but also across populations. Therefore, the deblending analysis was carried out on the full $K_{\rm vega} \leqslant 20$ sample. In doing so we have ignored sources with $K_{\rm vega} > 20$, and they have therefore not been included in the deblending analysis. In the following section, however, we show that these fainter sources do indeed make a contribution to the submm signal, which must be subtracted from the stacked fluxes. For an extensive comparative analysis of different stacking techniques (including the one presented here) and Monte Carlo simulations that demonstrate the convergence of our deblending method with those of other deblending/stacking methods, we refer to Kurczynski & Gawiser (2010).

4.3. Stacking the Full Samples

For each source in the $K_{\rm vega} \leqslant 20$ sample the (deblended) signal and noise values at its pixel position in the LABOCA map were recorded, and from those the stacked 870 μm flux density of the full sample was determined according to Equations (1) and (2). The 870 μm signal and noise values corresponding to the BzK, ERO, and DRG samples were extracted and their stacked 870 μm flux densities were derived in a similar manner. Also, postage stamp images around each source were extracted and combined in a weighted fashion resulting in stacked submm images of the K-selected samples (Figure 6). From the azimuthally averaged radial profiles of the submm signal, it is clear that the baseline level is not zero, but in fact there is a residual signal amounting to 0.065 mJy. While this baseline level probably stems from the population of the $K_{\rm vega} > 20$ galaxies lying below the submm detection limit of the LABOCA map, we stress that the residual signal will be affected by the subtraction of large-scale structure in the map described in Section 2. In order to account for the residual signal, the stacked 870 μm flux densities had a constant signal of 0.065 mJy subtracted from them. The final stacked 870 μm flux densities (with the 0.065 mJy baseline level subtracted) are given in Table 2. As a comparison, we also derived the median flux densities from the stacks and found agreement (to within 15%) with the weighted averages.

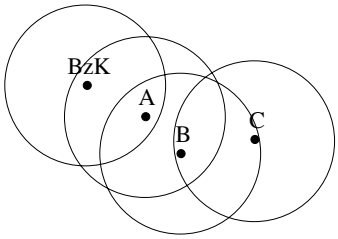

Figure 5. Example of where four sources form a "chain" of neighbors that need to be deblended. In order to properly calculate the 870 μm flux coming from the BzK galaxy at its position we have to calculate A's contribution, which in turn is affected by B, which in turn is affected by C. The "chain" stops here as C does not have any additional neighbors. In total, therefore, a linear set of four equations has to be solved (see Equations (3)–(6)). Each circle illustrate the "footprint" of the LABOCA beam. The longest such "chain" in our analysis involved 39 sources.

We find that all of our K-selected samples have very significantly ($\gtrsim 8\sigma$) detected stacked 870 μm fluxes, except for the pBzKs, which are detected only at the $\sim 3\sigma$ level. To gauge the significance of our results, we ran a series of Monte Carlo simulations in which stacking analyses were carried out on 1000 versions of the $K_{\rm vega} \leqslant 20$ catalog, each with randomized positions with respect to the original catalog. Each source was assigned a random position by (randomly) choosing a radius ($60'' \leqslant r \leqslant 200''$) and an angle from its original position. By confining the new positions to within a certain distance of the original, we ensured that the noise properties were similar to those in the original stacking analysis. As expected, the distributions of stacked signals obtained from these simulations were Gaussians centered on zero. We found that the measured 870 μm signals occurred in $<$0.05% of the simulation runs. Roughly, the same percentage is found if we restrict our Monte Carlo analysis to the sBzK, pBzK, ERO, and DRG samples, and clearly testify to the significance of the measured signals for these subsets.

From Table 2 it is seen that while the significance of the pBzK stacked signal is only $\sim 3\sigma$, the actual signal (0.28 ± 0.10 mJy) is in fact identical to that of the EROs (0.29 ± 0.03 mJy). It is possible, therefore, that the low significance of the stacked pBzK signal is partly due to the smaller sample size (and hence higher noise in the stack) rather than pBzKs being intrinsically devoid of submm emission. In order to test this we extracted random subsets of 147 EROs and stacked their fluxes. Doing so 1000 times, we found that in 10% of the cases a flux equal or smaller than that of the pBzKs was obtained. The average flux over the 1000 runs was 0.29 ± 0.10 mJy (S/N = 2.9), which is virtually identical to the stacking signal obtained for the pBzK galaxies. The fact that there is a 10% chance of obtaining a

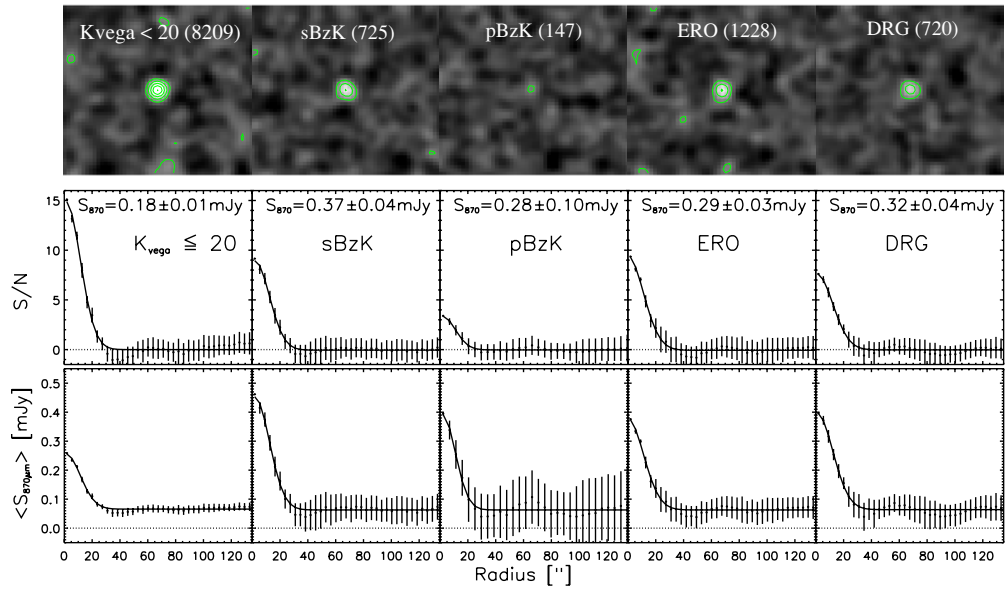

Figure 6. Top row: postage stamps of the stacked signal-to-noise images of the $K_{\rm vega} \leqslant 20$, BzK, ERO, and DRG samples. The contours start at S/N = 3 and increase in steps of three. The number of sources in each stack is given in parentheses. The angular resolution (FWHM = 27″) is shown as an insert in the left-hand panel. Middle row: radial profiles (azimuthally averaged) of the corresponding stacked S/N images (filled symbols). Gaussian fits to the profiles are indicated by the solid curve. Bottom row: radial profiles (azimuthally averaged) of the corresponding stacked signal images (filled symbols). Gaussian fits to the profiles are indicated by the solid curve. Note the non-zero baseline level (0.065 mJy) caused by the $K_{\rm vega} > 20$ sources with submm fluxes below the detection threshold. This constant baseline level has been removed from the S/N images and profiles in the top and middle panels.

signal corresponding to that of the pBzK by randomly stacking 147 sBzKs suggest that the low-significance of the pBzK stack is at least in part due to the small sample size, and that the pBzK galaxies in fact have a non-zero submm signal.

In addition to the above stacking analysis, we compared the distributions of S/N values at the positions of the submm-faint, near-IR sources with the overall S/N distribution of the residual LABOCA map. From Figure 7, it is seen that the distributions for the $K_{\rm vega} \leqslant 20$, sBzK, pBzK, ERO, and DRG samples all appear to be biased toward positive S/N values, although a formal Kolmogorov–Smirnov (K-S) statistic suggests that in the case of the full $K_{\rm vega} \leqslant 20$ sample, this bias is not statistically significant. Interestingly, the pBzK distribution shows an excess toward positive S/N values, which seem to be statistically significant ($P_{\rm KS} = 0.003$). This is consistent with the above finding of a significant (at the $\sim 3\sigma$ level) stacked 870 μm signal from pBzKs.

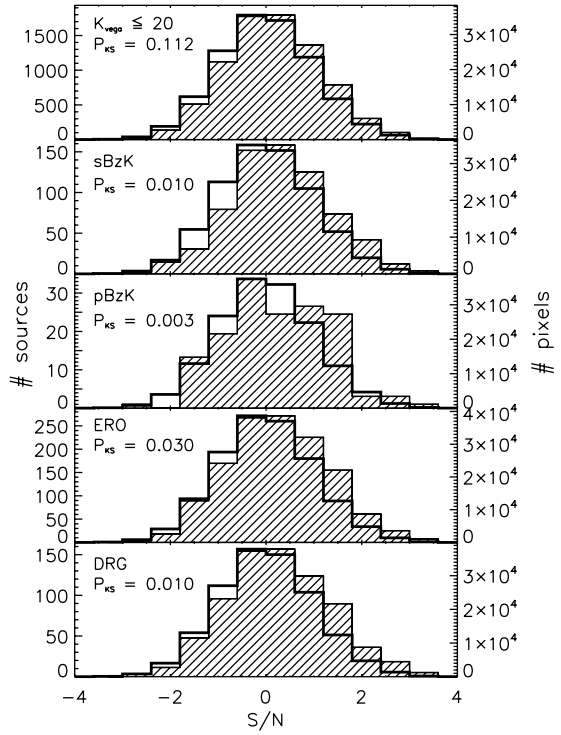

Figure 7. Distributions of the S/N values at the positions of the $K_{\rm vega} \leqslant 20$ BzK, ERO, and DRG samples (except for the ones associated with robust LABOCA sources, see Section 5.1), shown as hashed histograms from top to bottom, respectively. The open histograms show the S/N distribution of the residual LABOCA map. The map distribution has been binned to the same resolution as the sample distributions. The $P_{\rm KS}$ values are the likelihoods that the sample distributions are identical to the overall map distribution.

5. DISCUSSION

5.1. Stacked Submm Fluxes and Star Formation Rates

In Section 4, we found that all of our *K*-selected samples have highly significant ($\geqslant 8\sigma$) stacked 870 μm fluxes, except for the pBzKs which were only marginally detected ($\sim 3\sigma$). How do the stacked fluxes derived in Section 4 compare with previous submm stacking analyses of *K*-selected samples?

We find an average 870 μm flux density of 0.37 ± 0.04 mJy for our sample of submm-faint sBzK galaxies. In comparison, Daddi et al. (2005) estimated an average 850 μm signal of ~ 0.82 mJy (corresponding to a 870 μm signal of ~ 0.75 mJy[17]) for a sample of ~ 100 $K_{\rm vega} \leqslant 20$ submm-faint sBzK galaxies within the SCUBA map of GOODS-N. Takagi et al. (2007) reported an average 850 μm flux of 0.52 ± 0.19 mJy (corresponding to a 870 μm flux of 0.48 ± 0.18 mJy) from a sample of 112 $K_{\rm vega} \leqslant 20$ sBzK galaxies selected within the part

[17] We scale 850 μm fluxes to 870 μm fluxes assuming an optically thin, modified blackbody law with $\beta = 1.5$, such that: $S_{870\,\mu{\rm m}}/S_{850\,\mu{\rm m}} = (850\,\mu{\rm m}/870\,\mu{\rm m})^{2+\beta} = 0.92$.

Table 2
The Stacked 870 μm Flux Densities for the $K_{\rm vega} \leqslant 20$, BzK, ERO, and DRG Samples

Galaxy Type	$\langle S_{870\,\mu{\rm m}}\rangle$[a] (mJy)	$\langle S_{870\,\mu{\rm m}}\rangle$[b] (mJy)	δN[b] (sq. arcmin^{-1})	$\langle \delta I_{870\,\mu{\rm m}}\rangle$[b] (Jy sq. deg^{-1})
$K_{\rm vega} \leqslant 20$	0.18 ± 0.01 (8209, 18.0σ)	0.22 ± 0.01 (8266, 22.0σ)	9.18 ± 0.10	7.27 ± 0.34 ($16.5 \pm 5.7\%$)
sBzK	0.37 ± 0.04 (725, 9.3σ)	0.50 ± 0.04 (744, 12.5σ)	0.83 ± 0.03	1.49 ± 0.22 ($3.4 \pm 1.3\%$)
pBzK	0.28 ± 0.10 (147, 2.8σ)	0.34 ± 0.10 (149, 3.4σ)	0.17 ± 0.01	0.20 ± 0.14 ($0.5 \pm 0.3\%$)
sBzK+pBzK	0.35 ± 0.04 (872, 8.8σ)	0.48 ± 0.04 (893, 12.0σ)	0.99 ± 0.03	1.71 ± 0.23 ($3.9 \pm 1.4\%$)
ERO	0.29 ± 0.03 (1228, 9.7σ)	0.39 ± 0.03 (1253, 13.0σ)	1.39 ± 0.04	1.95 ± 0.21 ($4.4 \pm 1.6\%$)
DRG	0.32 ± 0.04 (720, 8.0σ)	0.43 ± 0.04 (737, 10.8σ)	0.82 ± 0.03	1.27 ± 0.20 ($2.9 \pm 1.1\%$)
BzK/ERO/DRG[c]	0.30 ± 0.03 (1961, 10.0σ)	0.39 ± 0.03 (1997, 13.0σ)	2.22 ± 0.05	3.12 ± 0.28 ($7.1 \pm 2.5\%$)
non-BzK/ERO/DRG[d]	0.14 ± 0.01 (6248, 14.0σ)	0.16 ± 0.01 (6269, 16.0σ)	6.97 ± 0.09	4.01 ± 0.26 ($9.1 \pm 3.2\%$)
$z < 1.4$				
$K_{\rm vega} \leqslant 20$	0.12 ± 0.01 (7023, 12.0σ)	0.18 ± 0.01 (7055, 18.0σ)	7.83 ± 0.09	5.08 ± 0.29 ($11.0 \pm 3.9\%$)
sBzK	0.28 ± 0.09 (162, 3.1σ)	0.34 ± 0.09 (164, 3.8σ)	0.18 ± 0.01	0.22 ± 0.14 ($0.5 \pm 0.2\%$)
pBzK	0.04 ± 0.17 (47, 0.24σ)	0.26 ± 0.17 (49, 1.5σ)	0.05 ± 0.01	0.05 ± 0.10 ($0.1 \pm 0.2\%$)
ERO	0.22 ± 0.04 (741, 5.5σ)	0.29 ± 0.04 (751, 7.3σ)	0.83 ± 0.03	0.87 ± 0.16 ($1.9 \pm 0.7\%$)
DRG	0.24 ± 0.06 (352, 4.0σ)	0.31 ± 0.06 (357, 5.2σ)	0.40 ± 0.02	0.44 ± 0.14 ($0.9 \pm 0.5\%$)
$z > 1.4$				
$K_{\rm vega} \leqslant 20$	0.34 ± 0.03 (1186, 11.3σ)	0.45 ± 0.03 (1211, 15.0σ)	1.35 ± 0.04	2.18 ± 0.22 ($4.7 \pm 1.7\%$)
sBzK	0.40 ± 0.05 (563, 8.0σ)	0.55 ± 0.05 (580, 11.0σ)	0.64 ± 0.03	1.28 ± 0.23 ($2.8 \pm 1.1\%$)
pBzK	0.38 ± 0.12 (100, 3.2σ)	0.48 ± 0.11 (102, 4.4σ)	0.11 ± 0.01	0.20 ± 0.18 ($0.4 \pm 0.4\%$)
ERO	0.40 ± 0.05 (487, 8.0σ)	0.55 ± 0.05 (502, 11.0σ)	0.56 ± 0.02	1.10 ± 0.22 ($2.4 \pm 0.1\%$)
DRG	0.39 ± 0.06 (368, 6.5σ)	0.55 ± 0.06 (380, 9.2σ)	0.42 ± 0.02	0.84 ± 0.22 ($1.8 \pm 0.8\%$)
24-μm detected ($S_{24\,\mu{\rm m}} > 27\,\mu$Jy)				
sBzK	0.52 ± 0.05 (449, 10.4σ)	0.71 ± 0.05 (466, 14.2σ)	0.52 ± 0.02	1.32 ± 0.27 ($2.9 \pm 1.2\%$)
pBzK	0.35 ± 0.16 (52, 2.2σ)	0.43 ± 0.16 (53, 2.7σ)	0.06 ± 0.01	0.09 ± 0.16 ($0.2 \pm 0.4\%$)
ERO	0.53 ± 0.05 (492, 10.6σ)	0.71 ± 0.05 (511, 14.2σ)	0.57 ± 0.03	1.45 ± 0.28 ($3.2 \pm 1.3\%$)
DRG	0.51 ± 0.06 (381, 8.5σ)	0.75 ± 0.06 (400, 12.5σ)	0.44 ± 0.02	1.19 ± 0.28 ($2.6 \pm 1.1\%$)
24-μm faint ($S_{24\,\mu{\rm m}} < 27\,\mu$Jy)				
sBzK	0.11 ± 0.07 (276, 1.6σ)	0.14 ± 0.07 (278, 2.0σ)	0.31 ± 0.02	0.16 ± 0.09 ($0.3 \pm 0.2\%$)
pBzK	0.23 ± 0.12 (95, 1.9σ)	0.29 ± 0.12 (96, 2.4σ)	0.11 ± 0.01	0.11 ± 0.12 ($0.2 \pm 0.3\%$)
ERO	0.14 ± 0.04 (736, 3.5σ)	0.18 ± 0.04 (742, 4.5σ)	0.82 ± 0.03	0.53 ± 0.14 ($1.2 \pm 0.5\%$)
DRG	0.09 ± 0.06 (339, 1.5σ)	0.17 ± 0.06 (344, 2.8σ)	0.38 ± 0.02	0.23 ± 0.10 ($0.5 \pm 0.2\%$)

Notes. The numbers of sources going into each stack are given in parentheses along with the significance of the stacked signals. Surface densities and contribution to the 870 μm EBL are also listed.
[a] Submm-faint sources only.
[b] Submm-bright sources included.
[c] The combined BzK, ERO and DRG samples, where source overlap between the populations have been accounted for.

of the Subaru/XMM-Newton deep field (SXDF) covered by the SCUBA HAlf Degree Extragalactic Survey (SHADES). Finally, D09 stacked the 850 μm signal from 1421 $K_{\rm vega} \lesssim 21.7$ sBzK galaxies and found 0.53 ± 0.06 mJy (corresponding to 0.49 ± 0.06 mJy at 870 μm).

For the 147 submm-faint pBzK galaxies we derived an average 870 μm flux density of 0.28 ± 0.10 mJy. As discussed in Section 4.3, there is statistical evidence of a positive submm signal from the pBzK sample, and the lower significance of the signal can be ascribed to a smaller intrinsic signal and sample size. We note that D09 measured an average 850 μm flux of 0.22 ± 0.18 mJy (or 0.20 ± 0.17 mJy at 870 μm) for a sample of 147 $K_{\rm vega} \lesssim 21.7$ pBzK galaxies, which, although not statistically significant, is in agreement with our result.

For the EROs and DRGs, we find stacked 870 μm fluxes of 0.29 ± 0.03 mJy and 0.32 ± 0.04 mJy, respectively. Webb et al. (2004) used the Canada–UK Deep Submillimeter Survey 03 hr and 14 hr fields (CUDSS03 and CUDSS14, respectively) to perform an 850 μm stacking analysis of 164 $K_{\rm vega} \lesssim 20.7$ EROs in the two fields, and found a stacked signal for the entire ERO sample of $\langle S_{870\,\mu{\rm m}}\rangle = 0.52 \pm 0.09$ mJy. Similarly, Takagi et al. (2007) measured a stacked 870 μm signal of 0.49 ± 0.16 mJy from a sample of 201 $K_{\rm vega} \leqslant 20$ EROs selected within SXDF/SHADES. Turning to DRGs, Knudsen et al. (2005) obtained a stacked 850 μm signal of 0.74 ± 0.24 mJy from a sample of 25 $K_{\rm vega} \leqslant 22.5$, submm-faint DRGs (uncorrected for an average gravitational lens amplification of 20%). Converting to a 870 μm flux density and correcting for the lens amplification yields 0.54 ± 0.18 mJy. Takagi et al. (2007), using significantly shallower SCUBA maps, failed at detecting a significant 850 μm signal from an average of 67 $K_{\rm vega} \leqslant 20$, submm-faint DRGs ($\langle S_{870\mu{\rm m}}\rangle = 0.39 \pm 0.23$ mJy).

We conclude that, within the errors, the previous stacking studies agree well with our results. We also note that our study provides the first robust ($\sim 8\sigma$) detection of submm-faint DRGs.

From the stacked submm fluxes we are able to estimate average IR luminosities and SFRs (Table 3). IR luminosities are derived by adopting the IR-to-submm SED of Arp 220 and scaling it to the stacked submm fluxes (at the median redshifts derived from the redshift distributions in Section 3.2) and integrating it from 8 to 1000 μm. For comparison, we also derive IR luminosities assuming that the SEDs are described by modified blackbody law with a dust temperature of $T_{\rm d} = 30$ K and $\beta = 1.5$, and integrating from 8 to 1000 μm. SFRs are

Table 3
The Average IR Luminosities and Star Formation Rates of BzK, ERO, and DRG Galaxies, Derived from their Stacked 870 μm Fluxes

Galaxy Type	$\langle z \rangle$	L_{IR}[a] (Arp 220) ($\times 10^{11} L_\odot$)	SFR[b] (Arp 220) ($M_\odot$ yr^{-1})	L_{IR}[a] ($T_d = 30$ K, $\beta = 1.5$) ($\times 10^{11} L_\odot$)	SFR[b] ($T_d = 30$ K, $\beta = 1.5$) ($M_\odot$ yr^{-1})
sBzK	1.8	5.0 ± 0.4	87 ± 7	1.8 ± 0.2	32 ± 3
pBzK	1.6	3.4 ± 1.6	58 ± 28	1.2 ± 0.4	21 ± 6
ERO	1.3	3.6 ± 0.3	63 ± 5	1.3 ± 0.1	23 ± 2
DRG	1.4	4.1 ± 0.4	71 ± 7	1.5 ± 0.1	26 ± 3
sBzK ($z < 1.4$)	1.1	2.9 ± 0.8	51 ± 14	1.1 ± 0.3	19 ± 5
sBzK ($z > 1.4$)	2.0	5.6 ± 0.5	96 ± 9	2.1 ± 0.2	36 ± 3
pBzK ($z < 1.4$)	1.2	2.3 ± 1.6	41 ± 26	0.9 ± 0.6	15 ± 10
pBzK ($z > 1.4$)	1.9	4.8 ± 1.1	84 ± 19	1.8 ± 0.4	32 ± 7
ERO ($z < 1.4$)	1.1	2.5 ± 0.3	43 ± 6	0.9 ± 0.1	16 ± 2
ERO ($z > 1.4$)	2.1	5.5 ± 0.6	96 ± 8	2.1 ± 0.2	37 ± 3
DRG ($z < 1.4$)	1.1	2.7 ± 0.5	46 ± 9	1.0 ± 0.2	17 ± 3
DRG ($z > 1.4$)	2.4	5.5 ± 0.6	94 ± 10	2.2 ± 0.2	38 ± 4

Notes.
[a] IR luminosities are obtained by integrating the SED over the wavelength range 8–1000 μm.
[b] SFRs are derived using SFR$[M_\odot\ \mathrm{yr}^{-1}] = 1.73 \times 10^{-10} L_{IR}[L_\odot]$ (Kennicutt 1998).

derived following Kennicutt (1998): SFR$[M_\odot\ \mathrm{yr}^{-1}] = 1.73 \times 10^{-10} L_{IR}[L_\odot]$. This conversion assumes a Salpeter initial mass function (Salpeter 1955). Of course, we stress that considerable uncertainty is associated with the derived IR luminosities and SFRs since they depend on the assumed SED and IMF.

The average IR luminosities and SFRs estimated here for the $K_{vega} \leqslant 20$ sBzK, ERO, and DRG galaxies on the basis of their stacked submm fluxes lie in the ranges $\sim$(1–6) $\times 10^{11}\ L_\odot$ and $\sim$20–110 $M_\odot$ yr^{-1}, i.e., comparable to those of luminous infrared galaxies (LIRGs; $L_{IR} \sim 10^{11}\ L_\odot$—Sanders & Mirabel 1996) in the local universe. For the sBzK galaxies, the average IR luminosity and SFR derived here are fully consistent with UV, 24 μm, and radio studies of these galaxies (Daddi et al. 2007). We find that the ERO and DRG populations have significantly lower IR luminosities (by $\sim$40%) than the sBzK galaxies. This is in part due to the fact that we have made no attempt to weed out passive EROs/DRGs in the stacking analysis, and the stacked submm flux from dusty, star-forming EROs/DRGs is likely to be significantly higher.

5.2. Stacking in Redshift Bins

Using the photometric redshifts obtained in Section 3.2 we can stack our samples into separate redshift bins, thereby allowing us to determine which redshifts are contributing the most to the stacked submm signals. Redshift bins were chosen so that they were larger than the typical redshift uncertainty, and provided roughly the same number of sources in each bin. The latter ensured that the same sensitivity was reached in each bin, thus allowing for a direct comparison. Figure 8 shows the average flux densities of the different samples as a function of redshift. We stress that due to the essentially flat selection function of submm surveys over the redshift range $1 \lesssim z \lesssim 8$ (Blain & Longair 1993), the comparison of stacked submm fluxes at different redshifts directly translates into a comparison between far-IR luminosities (and thus SFRs—Kennicutt 1998) between these redshift bins (to the extent that submm flux is a measure of far-IR luminosity).

The average submm signal from $K_{vega} \leqslant 20$ galaxies is found to be roughly constant ($\sim$0.1–0.2 mJy) out to $z \sim 1.4$, and consistent with the average flux density of the full sample (Table 2). At $z \sim 1.7$, however, the submm signal has increased to $\sim$0.4 mJy. The stacked submm fluxes of $z < 1.4$ and $z > 1.4$ $K_{vega} \leqslant 20$ sources are 0.18 ± 0.01 mJy and 0.45 ± 0.03 mJy, respectively (Table 2). A similar increase in the average submm flux at $z > 1.4$ is seen for the ERO and DRG populations. The average IR luminosities and SFR for $z > 1.4$ EROs ($L_{IR} \simeq 5.5 \times 10^{11}\ L_\odot$ and SFR $\simeq 96\ M_\odot$ yr^{-1}) are about 2× higher than for $z < 1.4$ EROs ($L_{IR} \simeq 2.5 \times 10^{11}\ L_\odot$ and SFR $\simeq$ $43\ M_\odot$ yr^{-1}), where we have adopted the IR luminosities and SFRs derived from the Arp 220 SED. A similar trend is seen for DRGs: $z > 1.4$ DRGs have on average $L_{IR} \simeq 5.5 \times 10^{11}\ L_\odot$ and SFR $\simeq 94\ M_\odot$ yr^{-1}, while $z < 1.4$ DRGs have $L_{IR} \simeq$ $2.7 \times 10^{11}\ L_\odot$ and SFR $\simeq 46\ M_\odot$ yr^{-1}. These findings also fit with the ERO and DRG redshift distributions (Figure 4), where we found evidence for two sub-populations separated at $z \sim 1.6$. Due to our magnitude cutoff at $K_{vega} \leqslant 20$, our samples are biased toward increasingly more massive galaxies at higher redshifts. The strong submm signal indicates that a substantial fraction of massive EROs/DRGs at $z > 1.4$ are actively star-forming galaxies and not old, red galaxies. The gradual drop in the average submm signals at $z > 2.5$ could be indicative of a decline in the star formation activity in EROs and DRGs at these higher redshifts or, alternatively, it could simply reflect a bias toward less dusty (and thus star-forming) galaxies since at redshifts >2.5 K-band observations start sampling the optical (rest-frame) emission.

Turning to the BzK galaxies, we find that sBzKs exhibit a positive and, within the error bars, constant 870 μm signal ($\sim$0.4 mJy) over the redshift range $1 \lesssim z \lesssim 3$. This supports the notion that the sBzK criterion selects star-forming galaxies across this redshift range, and that for our K-band magnitude limit of $K_{vega} \leqslant 20$, the distribution of SFRs of sBzK galaxies is roughly constant within this redshift range. In contrast, the pBzK galaxies show no evidence of significant submm signal in any redshift bin, which is consistent with these galaxies being devoid of significant star formation. D09 reported a 850 μm signal of 0.89 ± 0.34 mJy ($\sim 2.6\sigma$) for pBzKs at $z < 1.4$ but no significant signal for pBzKs at $z > 1.4$. They argued that the submm signal for $z < 1.4$ pBzK galaxies was due to contamination by star-forming galaxies at $z < 1.4$. In comparison, we find no significant stacked 870 μm signal (0.04 ± 0.17 mJy) for

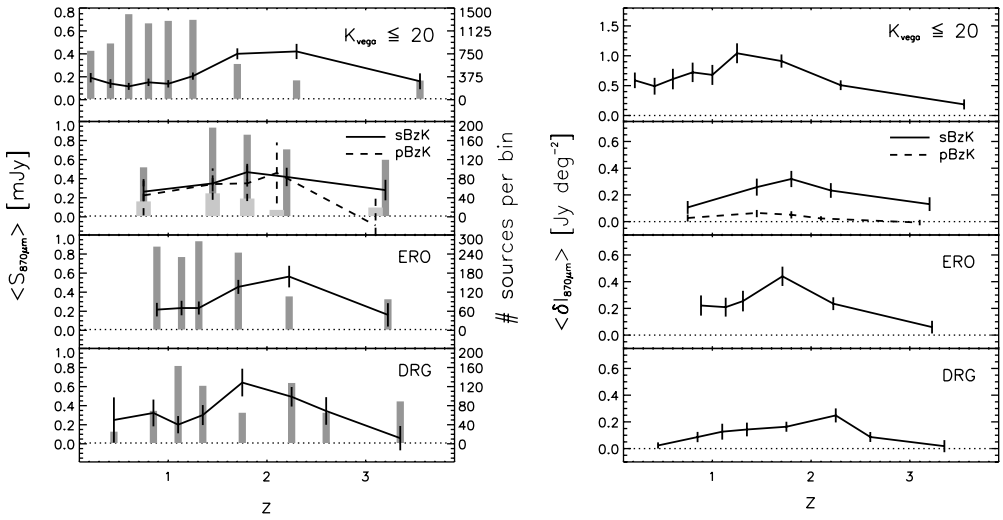

Figure 8. Stacked 870-μm flux densities (left panels) and the corresponding contribution to the 870-μm EBL (right panels) as a function of redshift for the $K_{\rm vega} \leqslant 20$, BzK, ERO and DRG samples. The gray histograms in the left hand panels indicate the number of sources in each bin (corresponding y-axis is on the right hand side). Broader, more light-gray histograms have been used for the pBzK galaxies.

$z < 1.4$ pBzKs and only a marginal signal for $z > 1.4$ pBzKs (0.38 ± 0.12 mJy).

5.3. Stacking in 24 μm Bins

Using the 24 μm source catalog from the FIDEL survey (which includes all sources $>27\,\mu$Jy, 5σ point-source sensitivity; Dickinson et al. 2007), a total of 466/53, 511, and 400 sources in the sBzK/pBzK, ERO, and DRG samples, respectively, were identified at 24 μm. Their average submm fluxes are given in Table 2 along with those of the 24 μm faint ($<27\,\mu$Jy) subsets. The 24 μm detected subsets have $\gtrsim 5\times$ higher average submm flux densities than the 24 μm faint sources. This is not surprising since the mid-IR is known to trace the thermal dust emission, and one might even expect a correlation between the submm and mid-IR emission.

In order to investigate the latter, we measured the stacked 870 μm signal as a function of 24 μm flux density bins (Figure 9). The sBzK, ERO, and DRG galaxies all exhibit a similar behavior, namely a significant linear correlation between the stacked 870 μm and 24 μm flux density up to $S_{24\,\mu{\rm m}} \simeq 350\,\mu$Jy, given by $\langle S_{870\,\mu{\rm m}}\rangle = 4.5 \times 10^{-3} \langle S_{24\,\mu{\rm m}}\rangle$, followed by a flattening of the relation for $S_{24\,\mu{\rm m}} > 350\,\mu$Jy. Not surprisingly, the pBzKs are not significantly detected at 870 μm in any of the 24 μm bins, and no submm-mid-IR correlation is seen.

Although the 24 μm selection function (Daddi et al. 2007) depends strongly on redshift (unlike the selection function at submm wavelengths), the observed $S_{24\,\mu{\rm m}}$–$S_{870\,\mu{\rm m}}$ correlation strongly suggests that 24 μm measurements (with $S_{24\,\mu{\rm mJy}} \gtrsim 350\,\mu$Jy) trace systems dominated by star formation, and can be used to derive IR luminosities and SFRs. The constant $S_{870\,\mu{\rm m}} \simeq 1.3$ mJy ratio for $S_{24\,\mu{\rm m}} \simeq 350$–$1000\,\mu$Jy either implies that these bright 24 μm sources are significantly contaminated by active galactic nucleus (AGN), which would boost the 24 μm signal but leave the 870 μm flux relatively unchanged, or that they are nearby ($z < 0.5$) sources in which case we would not expect them to exhibit a strong submm signal (due to the lack of a significant k-correction). The latter possibility can be ruled out, however, as a negligible fraction of the sources in our sample with $S_{24\,\mu{\rm m}} \geqslant 250\,\mu$Jy lie at $z < 0.8$. In fact, omitting these sources from the analysis does not change the $S_{24\,\mu{\rm m}}$–$S_{870\,\mu{\rm m}}$ correlation in any significant way.

It therefore seems most likely that the flattening of the correlation is due to the AGN contributing more prominently to the 24 μm flux in the brightest sources. Since the mid-IR will be more sensitive to warm dust ($T_{\rm d} \sim 80$–200 K) than the submm, which largely traces cold dust ($T_{\rm d} \sim 20$–60 K), the ability of the observed 24 μm emission to reliably trace IR luminosity and star formation may be compromised by AGN-heated warm dust. The turnover from a linear to a flat $S_{870\,\mu{\rm m}}$–$S_{24\,\mu{\rm m}}$ relation occurs at $S_{24\,\mu{\rm m}} \simeq 350\,\mu$Jy, which corresponds to $L_{\rm IR} < 1.5 \times 10^{12}\,L_\odot$ at $z \sim 2$.

Our findings are in line with those of Papovich et al. (2007), who found that IR luminosities derived from 24, 70, and 160 μm *Spitzer* data (of a sample of K-selected galaxies at $1.5 \lesssim z \lesssim 2.5$ with $S_{24\,\mu{\rm mJy}} \simeq 50$–$250\,\mu$Jy) were in good agreement with those derived from the 24 μm data alone. For sources with $S_{24\,\mu{\rm mJy}} > 250\,\mu$Jy, however, the latter would be $\sim$2–10$\times$ higher, suggesting that the AGN may contribute significantly to the high 24 μm emission. Similarly, Daddi et al. (2004, 2005) found that a large fraction ($>30\%$) of sBzK galaxies with $L_{\rm IR} \gtrsim 1.5 \times 10^{12}\,L_\odot$ (which corresponds to the IR luminosity where we find a turnover in the $S_{870\,\mu{\rm m}}$–$S_{24\,\mu{\rm m}}$ relation) show an excess of emission in the near-IR (rest frame) and are statistically detected in hard X-rays—evidence of powerful AGNs in these very IR-luminous systems.

5.4. Contributions to the Extragalactic Background Light

Turning to the contribution to the submm EBL by the different populations, we adopt the spectral approximations to the EBL at submm wavelengths from COBE/FIRAS (Puget et al. 1996; Fixsen et al. 1998), including their uncertainties. In doing so we adopt a value of the EBL at 870 μm of 44 ± 15 Jy deg^{-2}. From the surface densities of the samples we derive their contributions to the 870 μm EBL (Table 2). We find that the total contribution from all $K_{\rm vega} \leqslant 20$ sources to the 870 μm EBL is 7.27 ± 0.34 Jy deg^{-2} or $16.5\% \pm 5.7\%$. For the BzK galaxies we find that the passive ones contribute $\lesssim$1% to the 870 μm EBL, while the star-forming population contribute 1.49 ± 0.22 Jy deg^{-2}, corresponding to $3.4\% \pm 1.3\%$. The EROs contribute 1.95 ± 0.21 Jy deg^{-2} (or $4.4\% \pm 1.6\%$), while the

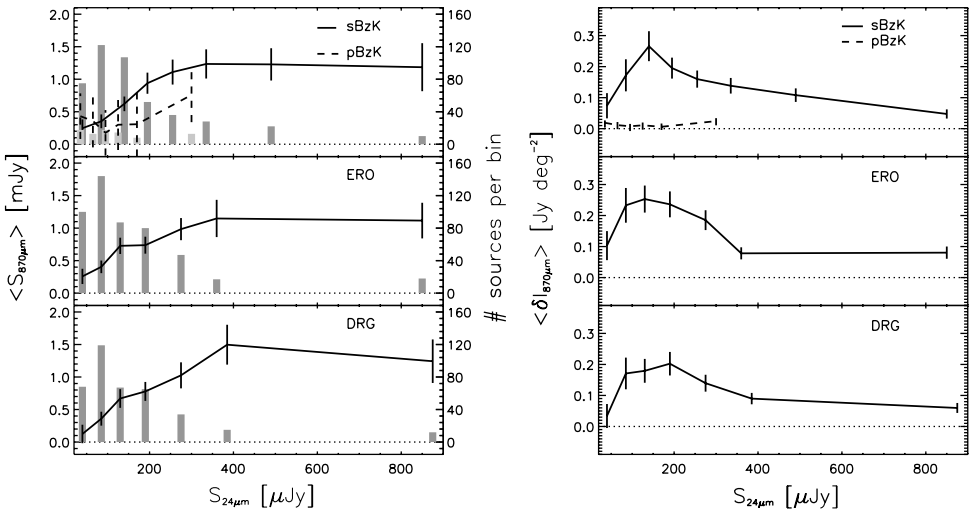

Figure 9. Stacked 870-μm flux densities (left panels) and the corresponding contribution to the 870-μm EBL (right panels) as a function of 24-μm flux density for the BzK, ERO, and DRG samples. The gray histograms in the left hand panels indicate the number of sources in each bin (corresponding y-axis is on the right hand side). Broader, more light-gray histograms have been used for the pBzK galaxies. In all cases, a significant $S_{870\,\mu m} - S_{24\,\mu m}$ correlation is found for $S_{24\,\mu m} \lesssim 350\,\mu$Jy, indicating that across this flux range, 24-μm observations trace star formation. For $S_{24\,\mu m} \gtrsim 350\,\mu$Jy, however, the relation flattens, suggestive of an increase in the fraction of AGN-dominated systems.

contribution from DRGs, owing to their lower surface density, is about 25% smaller (1.27 ± 0.20 Jy deg^{-2} or $2.9\% \pm 1.1\%$). The combined BzK/ERO/DRG sample contribute $7.1\% \pm 2.5\%$ to the EBL at 870 μm after accounting for overlap between the populations.

According to Takagi et al. (2007), sBzK galaxies down to $K_{\rm vega} \lesssim 20$ contribute 3.8 ± 1.2 Jy deg^{-2} (or $8.3\% \pm 3.9\%$) to the background light at 850 μm (46 ± 16 Jy deg^{-2}—Puget et al. 1996; Fixsen et al. 1998). Webb et al. (2004) found that the ERO population down to $K_{\rm vega} < 20.7$ constitutes 7%–11% of the EBL at 850 μm, while Takagi et al. (2007) reported a 850 μm EBL contribution from $K_{\rm vega} \lesssim 20$ EROs of 5.1 ± 1.5 Jy deg^{-2} ($11\% \pm 5\%$) to the total background at 850 μm. Knudsen et al. (2005) found that DRG galaxies down to $K_{\rm vega} < 22.5$ contribute $\sim$7.7 Jy deg^{-2} ($\sim$17%) of the EBL at 850 μm.

Next, let us look at the contribution to the EBL at 870 μm from the different samples as a function of redshift and 24 μm flux bins (right-hand panels in Figures 8 and 9). We calculate the contributions using the stacked submm flux and the surface density of sources in each redshift and 24 μm bin.

Looking at the redshift dependence first, we see that the single strongest contribution to the 870 μm EBL by $K_{\rm vega} \leqslant 20$ galaxies in a given redshift bin is coming from sources at $z \sim 1.4$. Sources at $z < 1.4$ contribute 3.3 ± 0.2 Jy deg^{-2} to the submm EBL, which corresponds to $\sim$45% of the total contribution from $K_{\rm vega} \leqslant 20$ galaxies (Table 2), and $\sim$11% of the total 870 μm EBL. $K_{\rm vega} \leqslant 20$ sources at $z > 1.4$ contribute only 2.18 ± 0.22 Jy deg^{-2} to the total EBL (or 30% of the total contribution from $K_{\rm vega} \leqslant 20$ galaxies). Although the $K_{\rm vega} \leqslant 20$ galaxies at $z > 2$ have significant submm emission (Section 5.2), their low abundance means that they contribute $\lesssim$1% to the observed submm EBL. In contrast, $z < 1$ $K_{\rm vega} \leqslant 20$ galaxies are so abundant (Figure 4) that despite their low average submm fluxes they contribute significantly to the submm EBL.

The bulk ($\sim$80%) of the contribution to the submm EBL from the 24 μm detected (i.e., $S_{24\,\mu Jy} > 27\,\mu$Jy) sBzK, ERO, and DRG galaxies comes from sources with $S_{24\,\mu Jy} \simeq 50$–$350\,\mu$Jy, with only a minor fraction coming from brighter, presumably, AGN-dominated sources.

5.5. Stacking Across the BzK and RJK Diagrams

The sBzK and pBzK selections are designed to locate star-forming and passive galaxies in the redshift range $1.4 \leqslant z \leqslant 2.5$, while the ERO and DRG color criteria are designed to select extremely red (either due to dust extinction or old age) galaxies at $z > 1$. Still, the exact definitions of these color criteria are somewhat arbitrary. Given the large number of sources available to us, we are in a position to construct stacks of the 870 μm signal from statistically significant subsets of galaxies across the BzK and RJK diagrams, thus allowing us to see where in these color–color diagrams the submm signal is coming from. Ultimately, this may allow us to fine-tune the sBzK/pBzK criteria, as well as potentially identify regions of the RJK diagram containing dusty/star-forming versus old/passive EROs and DRGs.

In Figures 10 and 11, we show the signal and S/N contours of the stacked 870 μm signal obtained across the BzK and RJK diagrams, where the stacking has been carried out within equally sized grid cells. We have done this for the full sample, as well as for subsets of the sample within the redshift intervals $0 < z < 0.8$, $0.8 < z < 1.5$, and $1.5 < z < 3.0$. These intervals were motivated by the redshift distributions in Figure 4, which showed evidence of distinct populations between $0.8 < z < 1.5$ and $1.5 < z < 3.0$.

Considering Figure 10(a) first, we see that the sBzK criterion by Daddi et al. (2004) seems to be robust in the sense that the strongest 870 μm signal is emerging from the sBzK region. Comparing with Figure 1(a) indicates that virtually the entire stacked submm signal from the sBzK galaxies is coming from the subset of sBzK galaxies (with a slight overlap into the pBzK and non-BzK regions), which have also been classified as EROs. Due to their extremely red colors and relatively strong submm signal, these galaxies are very likely to be among the most dusty, star-forming sources of the submm-faint $K_{\rm vega} \leqslant 20$ selected galaxies, yet their brightness ensures that they are detected in the blue (thus qualifying as sBzK galaxies).

The submm signal clearly extends into the pBzK region suggesting that some contamination by star-forming galaxies occurs. This is partly due the low density of sources in the

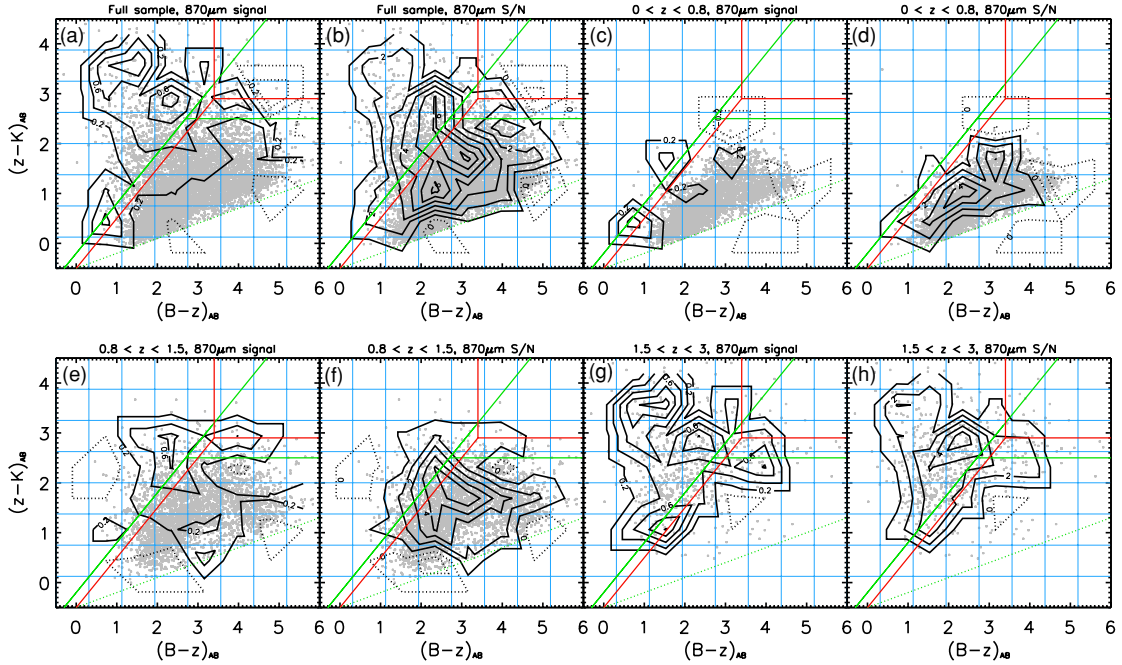

Figure 10. Contours of the average 870 μm signal per galaxy (in units of mJy) and S/N across the BzK diagram, obtained by stacking galaxies within regular grid cells (shown in blue). We have stacked the entire sample within the full redshift range, as well as subsets within the redshift ranges $z = 0$–0.8, 0.8–1.5, and 1.5–3.0. The sBzK and pBzK criteria by Daddi et al. (2004) are shown as solid green lines, while the refined selection criteria proposed in this paper are shown in red. The contours clearly supports the BzK-selection technique as the submm signal is seen to be almost entirely dominated by sBzK galaxies in the redshift range $z = 1.5$–3.

pBzK-region which implies that more sources will scatter into the region (due to photometric errors) than out of it. Based on the 870 μm signal and S/N contours in Figure 10, we propose a refinement of the sBzK and pBzK criteria, namely

$$(z - K)_{\rm AB} \geqslant (B - z)_{\rm AB} - 0.5, \quad (7)$$

$$(B - z)_{\rm AB} \leqslant 3.4 \quad (8)$$

for sBzKs, and

$$(z - K)_{\rm AB} \geqslant 2.9, \quad (9)$$

$$(B - z)_{\rm AB} > 3.4 \quad (10)$$

for pBzKs.

That these refined selection criteria might do a better job at selecting star-forming and passive BzK galaxies is confirmed if we consider how the submm signal across the BzK diagram changes with redshift (Figure 10 (c)–(h)). We find that only marginal 870 μm emission emerges from galaxies in the redshift interval $0 < z < 0.8$, while in the $0.8 < z < 1.5$ interval, significant submm emission ($\sim$0.6 mJy) starts to appear from galaxies lying within the sBzK region. At $1.5 < z < 3$ a strong submm signal ($\sim$1 mJy) and nearly all of the submm emission is coming from the sBzK region. This observed migration of the stacked submm signal toward the sBzK region as a function of redshift illustrates the ability of the sBzK criterion to select star-forming galaxies at $z \geqslant 1.5$. Stacking the 870 μm flux of the galaxies fulfilling the new pBzK criterion (only 17 sources in total) yields -0.10 ± 0.28 mJy, i.e., consistent with zero.

Turning to the RJK diagram, the bulk of the submm signal is found to come from the overlap region between DRGs and EROs, in particular from ERO/DRG galaxies with $(J-K)_{\rm AB} > 1.9$. The latter, together with the tentative evidence of an underdensity of sources at $(J - K)_{\rm AB} = 1.9$ (see Figure 1), suggests that $(J - K)_{\rm AB} > 1.9$ may be a useful criterion for selecting dusty, star-forming galaxies. This is strengthened by the fact that the submm signal becomes even stronger and further concentrated toward the ERO/DRG overlap region if we consider only the subset of sources at $z = 1.5$–3 (Figure 11 (g)–(h)). In the redshift range $0.8 < z < 1.5$, the submm signal is much weaker ($\sim$0.6 mJy) and comes from ERO/DRG galaxies with $(J - K)_{\rm AB} < 1.9$.

It is well known that the $K_{\rm vega} \leqslant 20$ ERO population is a heterogeneous population, consisting of roughly a 50-50 mix of dusty, star-forming EROs and evolved, passive EROs (Dey et al. 1999; Cimatti et al. 1999; Mannucci et al. 2002). Pozzetti & Mannucci (2000) argued that a crude separation between the two types of EROs could be made based on the criterion $(J-K)_{\rm AB} = 0.34(R-K)_{\rm AB} - 0.22$ (and $(R-K_S)_{\rm AB} \geqslant 3.35$),[18] with dusty, star-forming EROs lying above the relation and old, passive EROs below it. While our stacking analysis lends some merit to the Pozzetti & Mannucci criterion, as the bulk of the submm signal is clearly found above it, significant submm emission is also detected in the passive ERO region (in particular for sources at $z > 1.5$), suggesting that blindly applying the criterion does not produce clean samples of star-forming and passive EROs (see also Smail et al. 2002b).

Finally, we caution that by adopting equally sized grid cells, some cells will contain a significantly larger number of sources than others, thereby introducing a potential skewing of the measured S/N across the diagrams (which is why we also show the variation of the average submm flux density across the diagrams). As a check on our results, we therefore adopted two alternative methods for binning the sources. First, an adaptive mesh was applied by requiring that no more than 200 sources were allowed within a given cell, and, second, the 50 nearest neighbors of each source were identified and stacked. Reassuringly, the two additional binning methods gave results in good agreement with the regular grid results.

[18] We have converted the Pozzetti & Mannucci criterion, which was in the vega system, into AB magnitudes.

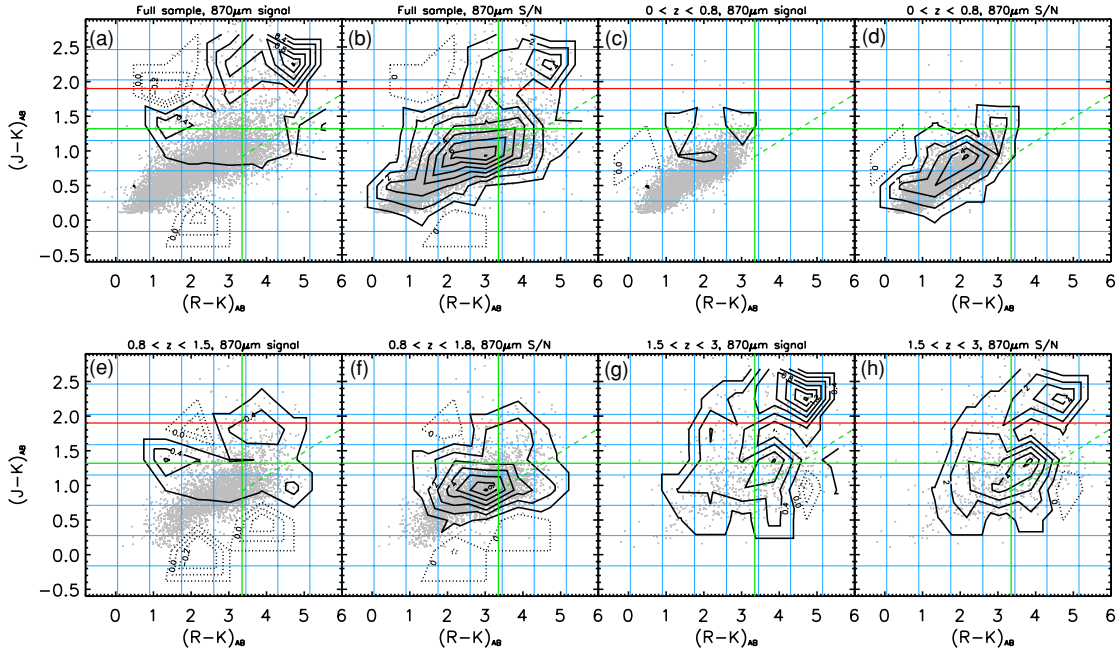

Figure 11. Contours of the average 870 μm signal per galaxy (in units of mJy) and S/N across the RJK diagram, obtained by stacking galaxies within regular grid cells (shown in blue). We have stacked the entire sample within the full redshift range, as well as subsets within the redshift ranges $z = 0$–0.8, 0.8–1.5, and 1.5–3.0. The ERO and DRG criteria are shown as vertical and horizontal solid green lines, while the star-forming vs. passive ERO criterion proposed by Pozzetti & Mannucci (2000) is illustrated by the green dashed line (with star-forming and passive EROs lying above and below the line, respectively). The strongest submm signal is coming from galaxies in the redshift range $z = 1.5$–3 lying in the DRG–ERO overlap region.

6. SUMMARY

Using the APEX/LABOCA 870 μm map of the ECDF-S (Weiß et al. 2009) along with the publicly available MUSYC survey data of this field (Taylor et al. 2009), we have performed a submm stacking analysis of 8266 *K*-band selected ($K_{\rm vega} \leqslant 20$) galaxies, as well as subsets of 737 DRG, 1253 ERO, and 744/149 sBzK/pBzK galaxies. Photometric redshifts have been derived for the full $K_{\rm vega} \leqslant 20$ sample using *UBVRIzJHK* data from MUSYC, thereby allowing us to study stacked submm flux densities as a function of redshift. This represents the largest submm stacking analyses of near-IR selected galaxies to date. The main results are summarized below.

1. We measure stacked 870 μm signals of 0.22 ± 0.01 mJy (22.0σ), 0.48 ± 0.04 mJy (12.0σ), 0.39 ± 0.03 mJy (13.0σ), and 0.43 ± 0.04 mJy (10.8σ) for the $K_{\rm vega} \leqslant 20$, BzK, ERO, and DRG samples, respectively. Splitting the BzK galaxies up into star-forming (sBzK) and passive (pBzK) galaxies, the former is significantly detected (0.50 ± 0.04 mJy, 12.5σ) while the latter, as expected, is only marginally detected (0.34 ± 0.10 mJy, 3.4σ). This implies that $K_{\rm vega} \leqslant 20$ galaxies are responsible for $16.5\% \pm 5.7\%$ of the EBL at 870 μm. sBzK galaxies, EROs, and DRGs (brighter than $K_{\rm vega} \leqslant 20$) are found to contribute $\sim$4% of the 870 μm background each.
2. Performing the stacking analysis in redshift bins, it is found that the stacked submm signal from $K_{\rm vega} \leqslant 20$ galaxies, as well as the ERO and DRG sub-samples, is coming from sources in the redshift range $1.4 \lesssim z \lesssim 2.5$, while for BzK galaxies the signal remains constant with redshift. Assessing the contribution to the submm EBL from the different samples as a function of redshift is complicated by the fact that these are flux-limited samples, although we can conclude that $\sim$45% of the contribution to the 870 μm EBL from $K_{\rm vega} \leqslant 20$ galaxies comes from sources at $z < 1.4$.
3. We find a linear correlation between stacked submm flux and 24 μm flux density for sBzK, ERO, and DRG galaxies with $S_{24\,\mu{\rm m}} \lesssim 350\,\mu$Jy. This correlation suggests that the 24 μm emission from the $S_{24\,\mu{\rm m}} \lesssim 350\,\mu$Jy galaxies is dominated by star formation, and consequently, can be used as a robust tracer of star formation. At $S_{24\,\mu{\rm m}} > 350\,\mu$Jy we find that the stacked 870 μm flux density becomes constant ($\sim$1.3 mJy) and independent of $S_{24\,\mu{\rm m}}$, which is likely due to AGNs starting to contribute significantly to the 24 μm as well as 870 μm emission.
4. In an effort to isolate a subset of BzK, ERO, and DRG galaxies responsible for the bulk of the stacked 870 μm emission we have measured the significance of the stacked submm signal across the BzK and RJK diagrams, identifying the regions of strongest submm emission. We find that the stacked submm signal from submm-faint sBzK galaxies is dominated by the subset of sources that also fulfill the ERO criterion. These are likely to be dusty, star-forming galaxies, which are sufficiently bright in the blue to be selected as sBzK galaxies. The majority of these sources are found in the redshift range $z = 1.5$–3, in line with the BzK-selection criterion proposed by Daddi et al. (2004). Guided by the stacked submm-contours we propose a slightly modified BzK-selection criteria, namely

$$(z - K)_{\rm AB} \geqslant (B - z)_{\rm AB} - 0.5, \quad (11)$$

$$(B - z)_{\rm AB} \leqslant 3.4 \quad (12)$$

for sBzKs, and

$$(z - K)_{\rm AB} \geqslant 2.9, \quad (13)$$

$$(B - z)_{\rm AB} > 3.4 \quad (14)$$

for pBzKs.

In the RJK diagram we find that the strongest submm signal comes from galaxies in the ERO/DRG overlap region with $(J - K)_{\rm AB} > 1.9$, which are predominantly found at $z \geqslant 1.5$.

We are grateful to Loretta Dunne and Ryan Quadri for providing us with the photometric redshift distributions published in D09 and Q07. I.R.S. acknowledges support from the Royal Society and STFC. T.R.G. is grateful to the European Southern Observatory (ESO) for sponsoring a four-month visit in Garching during which much of the analysis presented here was carried out, and would in particular like to thank Sune Toft, Carlos de Breuck, and Jesper Sommer-Larsen for useful discussions and suggestions during this period.

REFERENCES

Alexander, D. M., et al. 2003, AJ, 126, 539
Barger, A. J., Cowie, L. L., & Sanders, D. B. 1999, ApJ, 518, L5
Barger, A. J., Cowie, L. L., Sanders, D. B., Fulton, E., Taniguchi, Y., Sato, Y., Kawara, K., & Okuda, H. 1998, Nature, 394, 248
Bertoldi, F., et al. 2007, ApJS, 172, 132
Blain, A. W., & Longair, M. S. 1993, MNRAS, 264, 509
Blain, A. W., Smail, I., Ivison, R. J., Kneib, J.-P., & Frayer, D. T. 2002, Phys. Rep., 369, 111
Blain, A. W., et al. 1999, ApJ, 512, L87
Bolzonella, M., Miralles, J.-M., & Pellò, R. 2000, A&A, 363, 476
Brammer, G. B., van Dokkum, P. G., & Coppi, P. 2008, ApJ, 686, 1503
Chapman, S. C., Blain, A. W., Ivison, R. J., & Smail, I. 2003, Nature, 422, 695
Chapman, S. C., Blain, A. W., Smail, I., & Ivison, R. J. 2005, ApJ, 622, 772
Chapman, S. C., Scott, D., Borys, C., & Fahlman, G. G. 2002, MNRAS, 330, 92
Cimatti, A., et al. 1999, A&A, 352, L45
Cimatti, A., et al. 2002, A&A, 391, L1
Cimatti, A., et al. 2003, A&A, 412, L1
Cimatti, A., et al. 2008, A&A, 482, 21
Coppin, K., et al. 2006, MNRAS, 372, 1621
Coppin, K., et al. 2009, MNRAS, 395, 1905
Cowie, L. L., Barger, A. J., & Kneib, J. P. 2002, AJ, 123, 2197
Daddi, E., et al. 2004, ApJ, 617, 746
Daddi, E., et al. 2005, ApJ, 631, L13
Daddi, E., et al. 2007, ApJ, 670, 156
Damen, M., et al. 2009, ApJ, 690, 937
Dey, A., Graham, J., Ivison, R. J., Smail, I., Wright, G. S., & Liu, M. C. 1999, ApJ, 519, 610
Dickinson, M., et al. 2007, A&AS, 211, 5261
Dunne, L., et al. 2009, MNRAS, 394, 3
Elston, R., Rieke, G. H., & Rieke, M. J. 1988, ApJ, 331, L77
Fixsen, D. J., Dwek, E., Mather, J. C., Bennett, C. L., & Shafer, R. A. 1998, ApJ, 508, 123
Franx, M., et al. 2003, ApJ, 587, L79
Gawiser, E., et al. 2003, A&AS, 203, 2601
Gawiser, E., et al. 2006, ApJS, 162, 1
Giavalisco, M., et al. 2004, ApJ, 600, L93
Grazian, A., et al. 2007, A&A, 465, 393
Holland, W. S., et al. 1999, MNRAS, 303, 659
Hu, E. M., & Ridgway, S. E. 1994, AJ, 107, 1303
Hughes, D. H., et al. 1998, Nature, 394, 241
Kennicutt, R. C. 1998, ApJ, 498, 541
Knudsen, K. K., van der Werf, P. P., & Kneib, J.-P. 2008, MNRAS, 384, 1611
Knudsen, K. K., et al. 2005, ApJ, 632, L9
Kriek, M., et al. 2006, ApJ, 649, L71
Kriek, M., et al. 2008, ApJ, 677, 219
Kurczynski, P., & Gawiser, E. 2010, AJ, 139, 1592
Lane, K. P., et al. 2007, MNRAS, 379, L25
Lawrence, A., et al. 2007, MNRAS, 379, 1599
Lehmer, B. D., et al. 2005, ApJS, 161, 21
Luo, B., et al. 2008, ApJS, 179, L19
Mannucci, F., Pozzetti, L., Thompson, D., Oliva, E., Baffa, C., Comoretto, G., Gennari, S., & Lisi, F. 2002, MNRAS, 329, L57
McCarthy, P. J., Persson, S. E., & West, S. C. 1992, ApJ, 386, 52
Papovich, C., et al. 2007, ApJ, 668, 45
Popesso, P., et al. 2009, A&A, 494, 443
Pozzetti, L., & Mannucci, F. 2000, MNRAS, 317, L17
Puget, J.-L., Abergel, A., Bernard, J.-P., Boulanger, F., Burton, W. B., Desert, F.-X., & Hartmann, D. 1996, A&A, 308, L5
Quadri, R., et al. 2007, AJ, 134, 1103
Reddy, N. A., Erb, D. K., Steidel, C. C., Shapley, A. E., Adelberger, K. L., & Pettini, M. 2005, ApJ, 633, 748
Rix, H.-W., et al. 2004, ApJS, 152, 163
Salpeter, E. E. 1955, ApJ, 121, 161
Sanders, D. B., & Mirabel, I. F. 1996, ARA&A, 34, 749
Siringo, G., et al. 2009, A&A, 497, 945
Smail, I., Ivison, R. J., & Blain, A. W. 1997, ApJ, 490, L5
Smail, I., Ivison, R. J., Blain, A. W., & Kneib, J.-P. 2002a, MNRAS, 331, 495
Smail, I., Owen, F. N., Morrison, G. E., Keel, W. C., Ivison, R. J., & Ledlow, M. J. 2002b, ApJ, 581, 844
Spergel, D. N., et al. 2003, ApJS, 148, 175
Szokoly, G. P., et al. 2004, ApJS, 155, 271
Takagi, T., et al. 2007, MNRAS, 381, 1154
Taylor, E., et al. 2009, ApJS, 183, 295
van Dokkum, P. G., et al. 2003, ApJ, 587, L83
Vanzella, E., et al. 2005, A&A, 434, 53
Vanzella, E., et al. 2006, A&A, 454, 423
Vanzella, E., et al. 2008, A&A, 478, 83
Wang, W.-H., Cowie, L. L., & Barger, A. J. 2006, ApJ, 647, 74
Webb, T. M. A., Brodwin, M., Eales, S., & Lilly, S. J. 2004, ApJ, 605, 645
Weiß, A., et al. 2009, ApJ, 707, 1201
Wolf, C., Dye, S., Kleinheinrich, M., Meisenheimer, K., Rix, H.-W., & Wisotzki, L. 2001, A&A, 377, 442
Yan, L., Thompson, D., & Soifer, B. T. 2004, AJ, 127, 1274